Soft Matter

Non-Close-Packed Hexagonal Self-Assembly of Janus Nanoparticles on Planar Membranes

Journal:	*Soft Matter*
Manuscript ID	SM-ART-07-2023-000984.R1
Article Type:	Paper
Date Submitted by the Author:	18-Sep-2023
Complete List of Authors:	Zhu, Yu; The University of Memphis, Physics and Materials Science Sharma, Abash; The University of Memphis, Physics and Material Science Spangler, Eric; The University of Memphis, Physics Laradji, Mohamed; The University of Memphis, Physics and Materials Science

Soft Matter

ARTICLE TYPE

Cite this: DOI: 00.0000/xxxxxxxxxx

Non-Close-Packed Hexagonal Self-Assembly of Janus Nanoparticles on Planar Membranes †

Yu Zhu,[a] Abash Sharma,[a] Eric J. Spangler,[a] and Mohamed Laradji[a*]

Received Date
Accepted Date

DOI: 00.0000/xxxxxxxxxx

The adhesion modes of an ensemble of spherical Janus nanoparticles on planar membranes are investigated through large-scale molecular dynamics simulations of a coarse-grained implicit-solvent model. We found that the Janus nanoparticles adhering to planar membranes exhibit a rich phase behavior that depends on their adhesion energy density and areal number density. In particular, effective repulsive membrane-curvature-mediated interactions between the Janus nanoparticles lead to their self-assembly into an ordered hexagonal superlattice at intermediate densities and intermediate to high adhesion energy density, with a lattice constant determined by their areal density. The melting behavior of the hexagonal superlattice proceeds through a two-stage melting scenario in agreement with the Kosterlitz-Thouless-Halperin-Nelson-Young classical theory of two-dimensional melting.

1 Introduction

Recent studies have shown that nanoparticle (NP) assemblies can potentially be used in a range of advanced applications including energy harvesting,[1] energy storage,[2] non-linear optics,[3] biosensing,[4] catalysis,[5] imaging,[6] and drug delivery.[7] Assemblies of NPs can be synthesized through either top-down or bottom-up strategies. In top-down strategies, which include electron-beam lithography[8] and laser machining,[9,10] a material is typically ablated into the desired nanostructure. In contrast, bottom-up strategies are based on the spontaneous self-assembly of the NPs into specific structures. These self-assemblies result from effective interactions between the NPs mediated by materials such as block copolymers,[11] proteins,[12,13] polypeptides,[14] polysaccharides,[15] liquid crystals,[16] and RNA or DNA strands.[17,18] Nanoassemblies produced using bottom-up methods include dimers,[19] trimers,[20] tetramers,[21] icosamers,[22] pyramids,[23] tori,[24] chiral structures,[25,26] and hexagonal superlattices.[27]

Many experimental and computational studies have demonstrated that the adhesion of NPs with uniform surfaces to planar lipid membranes or lipid vesicles leads to effective interactions between them that are mediated by deformations in the membrane curvature.[28–36] These interactions often lead to the self-assembly of the NPs into in-plane linear chains or out-of-plane tubular chains.[28–30,32,33] These assemblies are characterized by the NPs being in contact with each other. Since many advanced applications require superlattices or clusters of NPs in which they are not necessarily in contact with each other, it would be very desirable to determine if lipid membranes can mediate the self-assembly of NPs such that they are not in contact with each other.

Recent simulations showed that surface modification of NPs into Janus NPs (JNPs), such as one moiety interacting attractively with the lipid head groups and the other interacting repulsively with the lipid membrane, causes repulsive membrane-mediated interactions.[37,38] More recently, we showed that due to this repulsive interaction, the adhesion of many spherical JNPs onto a lipid vesicle leads to their self-assembly into an array of highly ordered nanoclusters, with geometries determined by the number of JNPs on the vesicle. Furthermore, the nanoclusters polyhedra, whose vertices correspond to the JNPs centers and whose edges are determined by connecting each JNP to its nearest neighbors, satisfy the upper limit of Euler's polyhedral formula,[39] i.e., the average number of nearest neighbors per JNP is maximized.[40] In particular, we showed that four, six, and 12 JNPs self-assemble into Platonic solids corresponding to the regular tetrahedron, octahedron, and icosahedron, respectively. In contrast, eight and 20 JNPs do not self-assemble into their respective Platonic solids corresponding to the cube and dodecahedron since these polyhedra do not obey the upper limit of Euler's polyhedral formula.[40] Furthermore, we showed that the geometries of these nanoclusters are preserved for a given number of JNPs as the vesicle's diameter, D_{LV}, is increased, albeit the degree of fluctuations increases with D_{LV}.[40]

[a] Department of Physics and Materials Science, The University of Memphis, Memphis, TN 38152, USA
* mlaradji@memphis.edu

† Electronic Supplementary Information (ESI) available. See DOI: 10.1039/cXsm00000x/

The present work extends our recent study[40] to the limit of a large number of JNPs adhering to tensionless planar membranes as a function of the JNPs' number density and adhesion energy density. The study is achieved through systematic molecular dynamics simulations of a coarse-grained implicit-solvent model of self-assembled lipid membranes and tessellated nearly rigid JNPs.[38,40] The simulations show a rich phase behavior, which includes a disordered phase of dispersed JNPs on the membrane at low values of the adhesion energy density, ξ, or low values of the number density, ρ, and an ordered hexagonal superlattice of the JNPs at high ξ and intermediate ρ, in which the JNPs are apart from each other. The lattice constant of the self-assembled hexagonal lattice is determined by ρ. By analyzing various structural quantities, we found that the hexagonal lattice melts as ρ is decreased via an intermediate hexatic phase, in agreement with the Kosterlitz-Thouless-Halperin-Young-Nelson (KTHNY) classical theory of two-dimensional (2D) melting.[41–44]

2 Model and Methods

2.1 Modeling of the Lipid Bilayer and Janus Nanoparticles

In the present work, we use an implicit-solvent model of self-assembled lipid membranes,[45,46] in which a lipid molecule is coarse-grained into a short, semi-flexible chain composed of one head (h) bead and two tail (t) beads. The potential energy of the lipid bilayer is given by

$$U(\{\mathbf{r}_i\}) = \sum_{i,j} U_0^{\alpha_i\alpha_j}(r_{ij}) + \sum_{\langle i,j\rangle} U_{\rm bond}^{\alpha_i\alpha_j}(r_{ij}) + \sum_{\langle i,j,k\rangle} U_{\rm bend}^{\alpha_i\alpha_j\alpha_k}(\mathbf{r}_i,\mathbf{r}_j,\mathbf{r}_k), \quad (1)$$

where $\mathbf{r}_i$ is the coordinate of bead i, $r_{ij} = |\mathbf{r}_i - \mathbf{r}_j|$, and $\alpha_i = h$ or t if i is a head or tail bead, respectively. The angular bracket in the second summation of Eq. (1) denotes that i and j are bonded and belong to the same lipid chain. The angular bracket in the third summation denotes that i, j, and k are part of the same lipid chain.

In Eq. (1), $U_0^{\alpha\beta}$ is a soft two-body potential between beads of types α and β, and is given by

$$U_0^{\alpha\beta}(r) = \begin{cases} \left(u_M^{\alpha\beta} - u_m^{\alpha\beta}\right)\frac{(r_m - r)^2}{r_m^2} + u_m^{\alpha\beta} & \text{if } r \le r_m, \\ -2u_m^{\alpha\beta}\frac{(r_c - r)^3}{(r_c - r_m)^3} + 3u_m^{\alpha\beta}\frac{(r_c - r)^2}{(r_c - r_m)^2} & \text{if } r_m < r \le r_c, \\ 0 & \text{if } r > r_c, \end{cases} \quad (2)$$

where $u_M^{\alpha\beta} > 0$ and $u_m^{\alpha\beta} \le 0$ for any pair (α,β). $u_m^{\alpha\beta} = 0$ implies an entirely repulsive interaction between α and β, with a cutoff distance r_m. $u_m^{\alpha\beta} < 0$ implies a short-range attraction between i and j for $r_m < r \le r_c$. $u_m^{hh} = u_m^{ht} = 0$ and strong enough negative values of u_m^{tt} ensure that the lipid chains self-assemble into stable bilayers.[46] r_m also sets the size of a bead.

Consecutive beads in a lipid chain are connected by $U_{\rm bond}^{\alpha_i\alpha_j}$ in Eq. (1), which is given by

$$U_{\rm bond}^{\alpha_i\alpha_j}(r_{ij}) = \frac{k_{\rm bond}^{\alpha_i\alpha_j}}{2}\left(r_{ij} - b_{\alpha_i\alpha_j}\right)^2, \quad (3)$$

Table 1 Model interaction parameters.

Parameter	Value
u_M^{hh}, u_M^{ht}	100ε
u_m^{tt}	200ε
u_m^{hh}, u_m^{ht}	0
u_m^{tt}	-6ε
$u_M^{n_a h}$	200ε
$u_m^{n_a h}$	$-\mathscr{E}$
$u_M^{n_b h}$, $u_M^{n_b t}$, $u_M^{n_a t}$	100ε
$u_m^{n_b h}$, $u_m^{n_b t}$, $u_m^{n_a t}$	0
$u_M^{n_a n_a}$, $u_M^{n_a n_b}$, $u_M^{n_b n_b}$	200ε
$u_m^{n_a n_a}$, $u_m^{n_a n_b}$, $u_m^{n_b n_b}$	0
$k_{\rm bond}^{ht}$, $k_{\rm bond}^{tt}$	$100\varepsilon/r_m^2$
$k_{\rm bend}^{htt}$	100ε
$k_{\rm bond}^{nn}$	$1200\varepsilon/r_m^2$
$k_{\rm bond}^{nc}$	$45\varepsilon/r_m^2$
$k_{\rm bend}^{nnn}$	250ε
r_c	$2r_m$
b_{ht}, b_{tt}	$0.7r_m$
b_{cn}	$D/2$

where $k_{\rm bond}^{\alpha_i\alpha_j}$ is the bond stiffness coefficient, and $b_{\alpha_i\alpha_j}$ is the preferred bond length between beads i and j. We note that i and j also interact with each other through $U_0^{\alpha_i\alpha_j}$.

Lastly, to account for the semi-flexibility of a lipid chain, its three beads interact as well through a three-body potential $U_{\rm bend}^{\alpha_i\alpha_j\alpha_k}$, in Eq. (1), that is given by

$$U_{\rm bend}^{\alpha_i\alpha_j\alpha_k}(\mathbf{r}_i,\mathbf{r}_j,\mathbf{r}_k) = \frac{k_{\rm bend}^{\alpha_i\alpha_j\alpha_k}}{2}\left(\cos\varphi_0 - \frac{\mathbf{r}_{ij}\cdot\mathbf{r}_{kj}}{r_{ij}r_{kj}}\right)^2, \quad (4)$$

where $k_{\rm bend}^{htt}$ is the bending stiffness coefficient, and φ_0 is the preferred splay angle of the lipid chain, taken to be 180°.

JNPs are constructed as spherical tessellated shells in order to reduce their number of degrees while accounting for their Janusity. This is achieved by constructing a JNP as an icosahedron mesh followed by three subsequent triangulations, resulting in 642 nodes (beads of type n) and 1280 elementary triangles.[47] The nodes are then projected onto a sphere of diameter D, with the same center as the original icosahedron. Neighbouring beads of the JNP are connected by harmonic springs with the potential given by Eq. (3) with a bond stiffness $k_{\rm bond}^{nn}$ and a preferred bond length b_{nn}. To provide further rigidity to the JNP, the three-body interaction, given by Eq. (4) with a bending stiffness coefficient $k_{\rm bend}^{nnn}$, is added to every connected triplet of beads. The preferred values of the bond length, b_{nn}, and bond angle, φ_0^{nnn}, for a given JNP depend on the location of the beads on the JNP's surface and are determined from the initial configuration of the JNP following projection of the thrice-tessellated icosahedron on a sphere.[38] Since JNPs are hollow in this model, the two-body and three-body

interactions are insufficient to provide them with high rigidity unless $k_{\rm bond}^{nn}$ and $k_{\rm bend}^{nnn}$ are very high. However, this is not desirable since it would require very small time steps. This problem is mitigated by inserting an additional bead of type c at the center of a JNP and bonding it to all n beads of the JNP, by the harmonic potential given by Eq. (3), with a bond stiffness $k_{\rm bond}^{cn}$ and a preferred bond length $b_{cn} = D/2$.

A JNP is composed of two types of beads. These correspond to n_a-beads, which interact attractively with the h-beads through Eq. (2), i.e., with $u_u^{n_a h} < 0$, and n_b-beads, which interact repulsively with the h-beads, i.e., with $u_m^{n_b h} = 0$. Since these JNPs are not amphiphilic, both n_a and n_b-beads interact repulsively with the lipid t-beads, i.e., $u_m^{n_a t} = u_m^{n_b t} = 0$. This choice of interactions ensures that only n_a-beads tend to adhere to the membrane. To prevent aggregation of the JNPs in the solvent, beads belonging to different JNPs interact with each other repulsively through Eq. (2), i.e., $u_m^{n_a n_a} = u_m^{n_b n_b} = u_m^{n_a n_b} = 0$. In the remainder of the article, we will use the term Janusity (J) to define the area fraction of a JNP that interacts attractively with the lipid head groups, i.e., $J = d/D$, where d is the height of the spherical cap that interacts attractively with the lipid head beads. Fig. S1 (ESI†) depicts an equilibrated JNP with $J = 0.5$.

The interaction parameters used in the present study are shown in Table 1. The simulations are performed at $k_BT = 3.0\,\varepsilon$. With these parameters, the bending modulus of the bare bilayer, extracted from the spectrum of its height fluctuations, $\kappa \approx 30\,k_BT$.[46] This value is comparable to that of a DPPC bilayer in the fluid phase.[48] From comparison of the thickness of the present model bilayer in the fluid phase, which is very close to $4\,r_m$, with that of a typical fluid phospholipid bilayer (≈ 4 nm),[49] the small length scale $r_m \approx 1$ nm. In the remainder of the article, all length scales are then expressed in nanometers.

The interaction between a JNP and the lipid membrane is characterized by the adhesion energy density $\xi = |E_{adh}|/A_{adh}$, where E_{adh} is the net interaction energy between the NP and the membrane and A_{adh} is the area of JNP adhering to the membrane. A JNP n_a bead adheres to the membrane if it is within the interaction range r_c. A_{adh} is then the total area of the NP times the fraction of contact beads of the NP. Details of the calculation of ξ are found in ref.[38] and[50], and the dependence of ξ with the interaction parameter $\mathscr{E}$ is shown in Fig. S2 (ESI†).

The degree of wrapping of a JNP by the lipid membrane is defined by

$$W = \frac{1}{2}(1 - \cos\theta), \tag{5}$$

where the wrapping angle $\theta \in [0, \pi]$ is calculated as follows: For each azimuthal angle $\varphi \in [0, 2\pi)$, around the z-axis, a latitude angle $\theta_{\max}(\varphi)$ is determined as the maximum latitude angle of lipid head beads within the interaction range r_c from the NP's surface (see inset (1) of Fig. 1) . The wrapping angle θ is then defined as the average of $\theta_{\max}$ over φ. W is shown as a function of ξ, in Fig. 1, for the case of 20-nm JNPs with $J = 0.5$ and 1. This figure shows that in the case of a uniform NP ($J = 1$), W increases until complete wrapping and endocytosis at $\xi \approx 1.5 k_BT/\text{nm}^2$. However, in the case of $J = 0.5$, W increases rapidly with ξ as long as $W \lesssim J$, which corresponds to

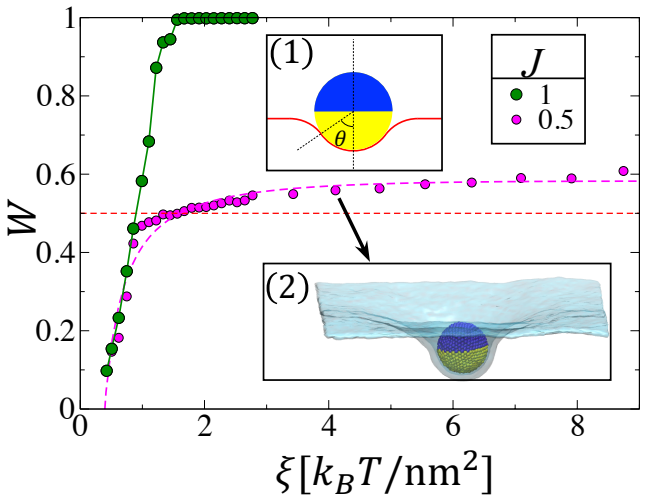

Fig. 1 Degree of wrapping W, defined by Eq. (5), versus ξ for different values of the Janusity J obtained from a simulation of a single 20-nm JNP on a planar tensionless lipid bilayer. Pink and green data points correspond to $J = 0.5$ and 1, respectively. The pink dashed line and the green solid line are guides to the eye in the case of $J = 0.5$ and 1, respectively. The red dashed line indicates a value of the degree of wrapping $W = 0.5$. Inset (1): Schematic definition of the degree of wrapping. Inset (2): Configuration of a JNP, with $J = 0.5$, and the membrane at $\xi = 4.11\,k_BT/\text{nm}^2$.

$\xi \lesssim 1\,k_BT/\text{nm}^2$. This is followed by a much weaker increase in W with ξ for $1\,k_BT/\text{nm}^2 \lesssim \xi \lesssim 2\,k_BT/\text{nm}^2$. W becomes almost independent of ξ at higher values of ξ. The intervals $\xi \lesssim 1\,k_BT/\text{nm}^2$, $1\,k_BT/\text{nm}^2 \lesssim \xi \lesssim 2\,k_BT/\text{nm}^2$ and $\xi \gtrsim 2\,k_BT/\text{nm}^2$ are termed the regimes of low, intermediate and high values of ξ, respectively.

2.2 Numerical Approach

The simulations are conducted through a hybrid approach, in which molecular dynamics is used to move the beads and Metropolis Monte Carlo is used to adjust the simulation box, with periodic boundary conditions along the three axes. More specifically, we use molecular dynamics with a Langevin thermostat to move all beads,[51]

$$\dot{\mathbf{r}}_i(t) = \mathbf{v}_i(t), \tag{6}$$

$$m\dot{\mathbf{v}}_i(t) = -\nabla_i U(\{\mathbf{r}_i\}) - \Gamma \mathbf{v}_i(t) + \sigma \Xi_i(t), \tag{7}$$

where $\mathbf{v}_i$ is the velocity of bead i and m is its mass (with the same value for all beads). Γ is a bead's friction coefficient (also with the same value for all beads), and $\sigma\Xi_i(t)$ is a random force acting on i originating from the heat bath. $\Xi_i(t)$ is a random vector that obeys $\langle \Xi_i(t) \rangle = 0$ and its components obey $\langle \Xi_i^{(\mu)}(t)\, \Xi_j^{(\nu)}(t') \rangle = \delta_{\mu\nu}\delta_{ij}\delta(t - t')$, where μ and $\nu = x$, y or z. The dissipative and random forces are interrelated through the dissipation-fluctuation theorem, which leads to $\Gamma = \sigma^2/2k_BT$, where k_B is Boltzmann's constant and T is temperature. Eqs. (6) and (7) are integrated using the velocity-Verlet algorithm[52] with $\Gamma = \sqrt{6}m/\tau$ and a time step $\Delta t = 0.02\tau$, where $\tau = r_m(m/\varepsilon)^{1/2}$.

The simulations are performed in the $NVT\gamma$ ensemble, where

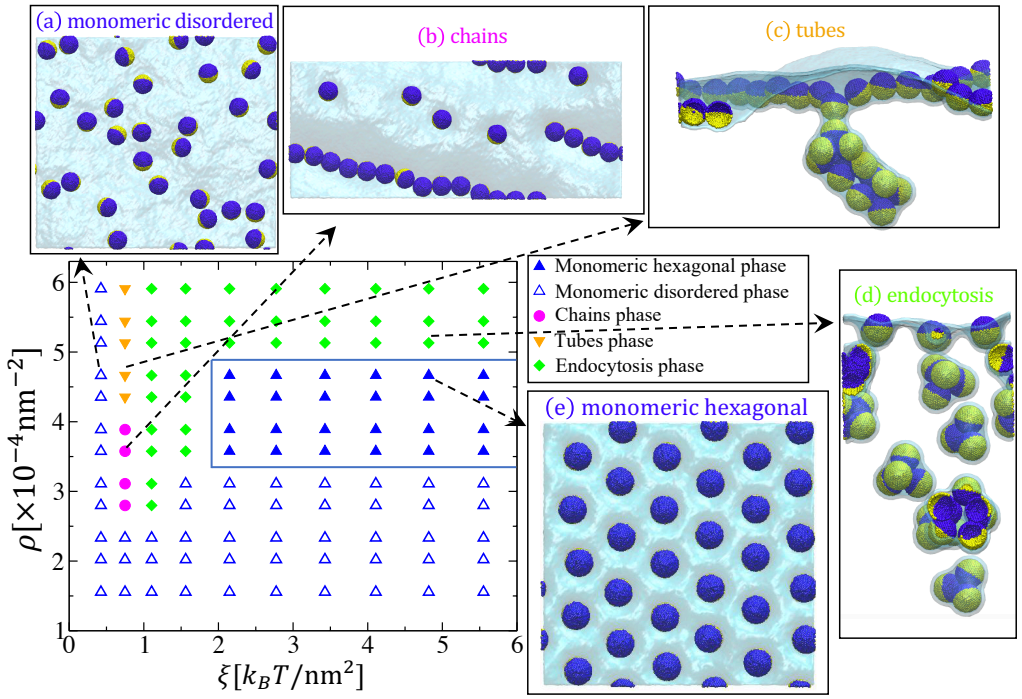

Fig. 2 Phase diagram of the JNPs arrangement on a tensionless planar membrane, showing the monomeric disordered phase (open blue triangles), monomeric hexagonal phase (solid blue triangles), in-plane chains phase (solid pink circles), tubes phase (orange triangles), and endocytosis phase (green diamonds). Snapshots (a) to (e) correspond to $(\rho(\times 10^{-4}\,\mathrm{nm}^{-2}), \xi(k_BT/\mathrm{nm}^2)) = (4.66, 0.425)$, $(3.576, 0.748)$, $(4.66, 0.748)$, $(5.13, 4.818)$, and $(4.66, 4.818)$, respectively.

γ is the surface tension, set to 0 since we focus on tensionless membranes in this work . N is the total number of beads in the system, and $V = L_xL_yL_z$ is the system's volume. The lipid membrane is overall parallel to the xy-plane. The Metropolis Monte Carlo scheme is used to adjust the system size along the xy-plane. Namely, for every 8 time steps, new values of the linear system sizes $L'_x = L_x + \Lambda_x$ and $L'_y = L_y + \Lambda_y$ are attempted, where Λ_x and Λ_y are small random perturbations in the interval $(-0.1r_m, 0.1r_m)$. Attempted new coordinates of all beads correspond then to $x'_i = x_i\left(\frac{L'_x}{L_x}\right)$, $y'_i = y_i\left(\frac{L'_y}{L_y}\right)$ and $z'_i = z_i\left(\frac{L_xL_y}{L'_xL'_y}\right)$. The attempt is then accepted or rejected through the Metropolis rejection criterion with the effective Hamiltonian $\mathscr{H} = \mathscr{U}_{\mathrm{net}}(\{\mathbf{r}_i\}) + \gamma L_xL_y$, where $\mathscr{U}_{\mathrm{net}}$ is the net potential energy of the system. The simulations are performed on tensionless membranes, $\gamma = 0$. In all simulations, if not specified, the number of lipid chains in the system is 199 172. This corresponds to a linear size of the bare tensionless bilayer about $L_x^{(0)} = 253.6$ nm. The JNPs diameter $D = 20$ nm, and their Janusity $J = 0.5$. The number of JNPs, n, is varied between 10 and 38. In the simulations, the JNPs are initially placed slightly above the equilibrated lipid membrane at random positions. The JNPs quickly adhere to the planar membrane. The system is typically equilibrated over a large number of steps (typically around $1.5 \times 10^6\,\tau$), and the results are collected once equilibrium is reached over a time scale ranging between 2×10^6 and $2 \times 10^7\,\tau$.

3 Results

3.1 Phase Diagram

An extensive set of simulations was performed, using the model and approach in Section 2, to determine the adhesion modes of many spherical JNPs on a tensionless lipid membrane. Fig. 2 depicts the obtained phase diagram in terms of the adhesion energy density, ξ, and the JNPs areal number density, $\rho = n/\mathscr{A}$, where n is the number of JNPs adhering to the membrane, and $\mathscr{A}$ is the projected area of the bare tensionless membrane. This figure demonstrates several adhesion modes. Namely, at low values of ξ or low values of ρ, the JNPs are dispersed into a monomeric disordered phase. Snapshot (a) in Fig. 2 depicts an example of this structure. At low values of ξ and intermediate values of ρ, the JNPs self-assemble into in-plane linear chains, with an example shown by snapshot (b) in Fig. 2. This phase is the result of the increased degree of wrapping of the JNPs with ξ, as shown in Fig. 1, and by their increased crowding with ρ. Further increased crowding, as ρ is further increased at low values of ξ, leads to the self-assembly of a fraction of the JNPs into out-of-plane chains coexisting with in-plane chains, as shown by snapshot (c) in Fig. 2.

At high values of ρ and intermediate to high values of ξ, the increased degree of wrapping of the JNPs by the membrane and increased crowding leads to their aggregation into compact clusters and their endocytosis, as shown by snapshot (d) in Fig. 2.

The absence of aggregation at low values of ρ, regardless of ξ, is inferred from free energy calculations using the weighted histogram analysis method (WHAM), in conjunction with many

umbrella sampling simulations of two JNPs with the following bias potential,[53]

$$U_{\rm bias}^{(d)}(R_{12}) = \frac{k_{\rm bias}^{(d)}}{2}(R_{12}-d_{\rm bias})^2, \quad (8)$$

where $R_{12}=|\mathbf{R}_2-\mathbf{R}_1|$, with $\mathbf{R}_1$ and $\mathbf{R}_2$ being the coordinates of the center beads of JNPs 1 and 2, respectively. $k_{\rm bias}^{(d)}$ is varied between 3.33 and $33.3\,k_BT$. The reaction coordinate, d, is the distance between the JNPs' centers, and $d_{\rm bias}$ is the preferred distance between them. The step in $d_{\rm bias}$ is chosen to be small enough to ensure an appreciable amount of overlap between consecutive umbrella sampling histograms of the distance between the JNPs centers d. We note that the orientations of the JNPs in the umbrella sampling simulations are not constrained. Fig. 3(A) shows that this free energy decreases monotonically with d, which implies that in the dilute regime, the membrane induces a repulsive interaction between the JNPs, regardless of the adhesion energy density. Furthermore, Fig. 3(A) shows that the effective interaction between two JNPs becomes increasingly more repulsive with increasing ξ. It is interesting to note that a closer look at the free energy at low values of ξ shows the existence of a small local minimum at $d\approx D_{NP}+1$ nm, as demonstrated by the inset of Fig. 3(A). However, the free energy of the dimerized state is higher than that of the undimerized states. Furthermore, the energy barrier from the dimeric state to the monomeric state at low values of ξ is only a few k_BTs. Therefore, the dimeric state at low values of ξ can only be transient.

To confirm the free energy calculations discussed above, we calculated the fraction of time, χ_d, during which at least a single pair of JNPs form a dimer. In other words, χ_d is the fraction of snapshots in which at least one dimer exists. Fig. 3(B), which depicts χ_d versus ξ at a low density corresponding to $\rho=2.33\times10^{-4}\text{nm}^{-2}$, demonstrates that the JNPs dimerize only at low values of ξ. The fraction of time of dimerization is, however, zero at $\xi\gtrsim 1\,k_BT/\text{nm}^2$. This finding nicely confirms the free energy shown in Fig. 3(A). The inset of Fig. 3(B) shows that the rate of dimerization increases with the JNPs' density at low values of ξ, although most of the JNPs remain non-dimerized. However, at high adhesion energy density, the JNPs do not dimerize. This implies that, at high adhesion energy density, the membrane-mediated repulsion between JNPs is strong enough to prevent their clustering, even at intermediate densities. As the density is further increased, increased crowding of the JNPs eventually leads to their clustering and their endocytosis.

It is interesting to note that both the free energy and χ_d, shown in Fig. 3, indicate that the metastable dimeric state occurs in the regime where the degree of wrapping of a JNP is dominated by ξ, as demonstrated by Fig. 1. Within the regime where the Janusity dominates the degree of wrapping, the effective membrane-curvature mediated interaction between the JNPs is entirely repulsive.

Since dimers are mostly unstable at low densities, the presence of chains and tube phases at higher densities ($\rho\gtrsim 2.5\times10^{-4}\,\text{nm}^{-2}$ must be due to many-body effects. To infer that JNPs form chains at intermediate values of ξ (pink symbols) rather than more compact clusters, we performed WHAM calculations of a chain of three JNPs with indexes 1, 2, and 3. The center beads of JNPs 1 and 2 are connected by a stiff harmonic spring with a spring constant equal to $333.3\,k_BT$ to keep the distance between connected JNPs about $D_{NP}+1$ nm. The centers of JNPs 2 and 3 are similarly linked. These artificial spring bonds are necessary since the simulations are performed on three JNPs only adhering to a large membrane, that is, at a low value of ρ, and as we have seen earlier, the JNPs do not cluster at such low densities. This WHAM calculation is based on the following bias potential,

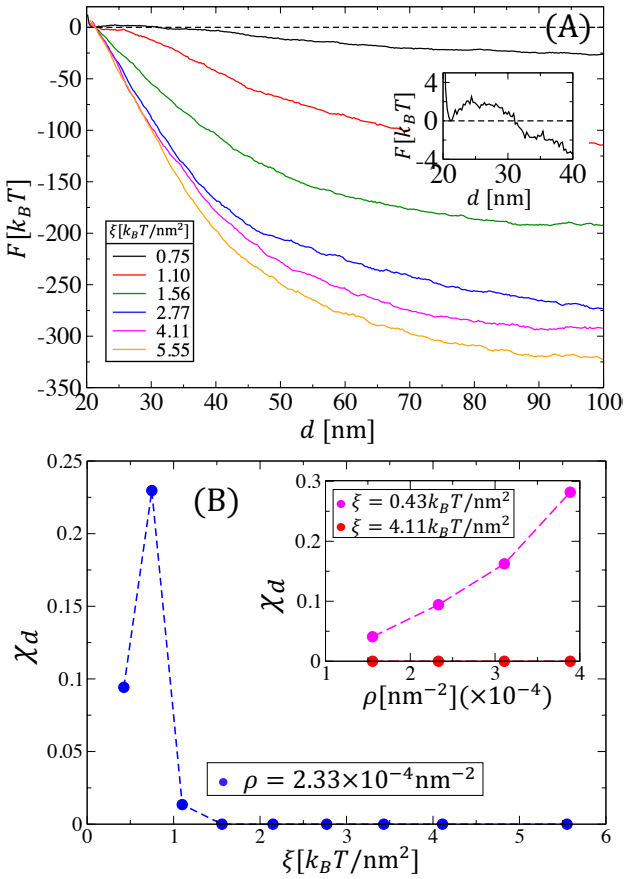

Fig. 3 (A) Free energy versus distance between two JNPs for different values of adhesion energy density. The horizontal dashed line corresponds to a free energy equal to 0. Insert: Zoom-in of the free energy for $\xi=0.75\,k_BT/\text{nm}^2$. (B) Fraction of time, χ_d, during which there is at least a single dimer in the system, versus adhesion energy density at a low density corresponding to $\rho=2.33\times10^{-4}\,\text{nm}^{-2}$. (Inset) χ_d versus density at a low and high value of the adhesion energy density. Note that at high values of the adhesion energy density, the JNPs do not dimerize at these densities.

$$U_{\rm bias}^{(a)}(\mathbf{r}_1,\mathbf{r}_2,\mathbf{r}_3) = \frac{k_{\rm bias}^{(a)}}{2}(\cos\theta-\cos\theta_0)^2, \quad (9)$$

where $k_{\rm bias}^{(a)}=333.3$ or $500\,k_BT$, and the reaction coordinate, $\theta=\cos^{-1}(\mathbf{R}_{12}\cdot\mathbf{R}_{32}/R_{12}R_{32})$, is the bond angle of the three JNPs. θ_0 is the preferred bond angle, and is varied between $\pi/3$, which corresponds to a tight equilateral aggregate and π , which corresponds

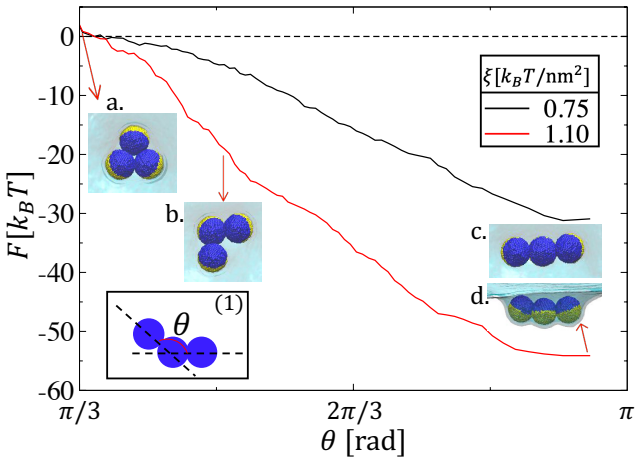

Fig. 4 Free energy versus the bond angle of three JNPs, which are linked by harmonic springs, as explained in the text. The bond angle is defined by Inset (1). The horizontal dashed line corresponds to a free energy equal to 0. (a), (b), and (c) are top view snapshots of the trimers obtained from the biased simulations, with a preferred bond angle equal to $\pi/3$, $\pi/2$ and almost π, respectively. (d) is a side view snapshot corresponding to (c).

to a linear aggregate. We note that the orientation of the JNP, as opposed to the orientation of the springs connecting them, is not fixed, and can vary due to the membrane fluctuations in each bias simulation. Therefore, we only focus on the bond angle of three NPs at this moment. Fig. 4 shows that this free energy is minimized at $\theta \approx \pi$. This implies that when three JNPs aggregate at intermediate densities, they prefer to form a chain rather than a compact equilateral triangle. The fact that the self-assembly of the JNPs into linear aggregates does not occur at low densities underscores the non-additive nature of the effective membrane-induced interaction between JNPs. This is not surprising since membrane deformations, induced by adhering JNPs, extend over length scales larger than the size of a JNP. As a result, the deformation of the membrane caused by a pair of JNPs leads to an effective interaction with a third JNP that is not merely the sum of the effective interactions due to individual JNPs of the pair.

For $\rho \gtrsim 4.4 \times 10^{-4}$ nm^{-2} and $\xi \approx 0.75 k_BT/\mathrm{nm}^2$, the JNPs self-assemble into tubules consisting of three linear chains apposed to each other, as shown by snapshot (c) in Fig. 2. These tubular chains occur at relatively high densities, as a result of crowding of the linear chains and their merger, ~~as shown by Movie 1,~~ tubular chains form as a result of merger of three linear chains. We note that the structure of these tubules differs from that of spherical NPs with uniform surfaces, which can form tubules with two apposed chains.[54] This is because tubes of two apposed chains require a relatively large degree of wrapping in the transverse direction compared to the case of three apposed chains. Since the NPs in the current study are Janus, transverse wrapping becomes limited by the Janusity. As such, a configuration of three apposed chains becomes more favorable.

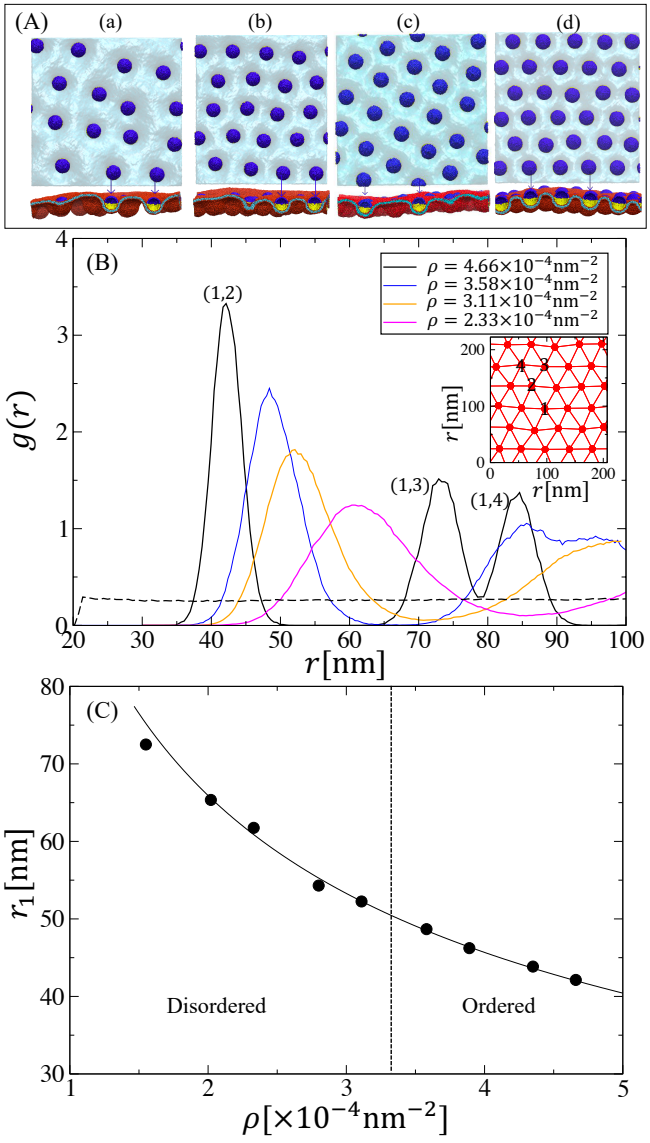

Fig. 5 (A) Top and side views of equilibrium configurations of the membrane with adhering JNPs for four density values at $\xi = 4.11 k_BT/\mathrm{nm}^2$. (a) to (d) correspond to $\rho = 2.33 \times 10^{-4}$, 3.11×10^{-4}, 3.58×10^{-4} and $4.66 \times 10^{-4}\,\mathrm{nm}^{-2}$, respectively. (B) The RDF, $g(r)$, of the JNPs centers of mass at $\xi = 4.11 k_BT/\mathrm{nm}^2$ and densities corresponding to snapshots (a)-(d) in (A). The dashed black line corresponds to the RDF at $\rho = 4.66 \times 10^{-4}\,\mathrm{nm}^{-2}$ and $\xi = 0.43 k_BT/\mathrm{nm}^2$, and demonstrates the very disordered structure of the JNPs at low adhesion energy density. (Inset) Centers beads of the JNPs connected to their nearest neighbors, using the Delaunay triangulation at $\rho = 4.66 \times 10^{-4}\,\mathrm{nm}^{-2}$ and $\xi = 4.11 k_BT/\mathrm{nm}^2$. (C) The distance between nearest neighbor JNPs (position of the first peak of the RDF) versus density. The solid line is a fit with the equation $r_1 = \alpha\sqrt{1/\rho - a}$, where α and a are positive constants.

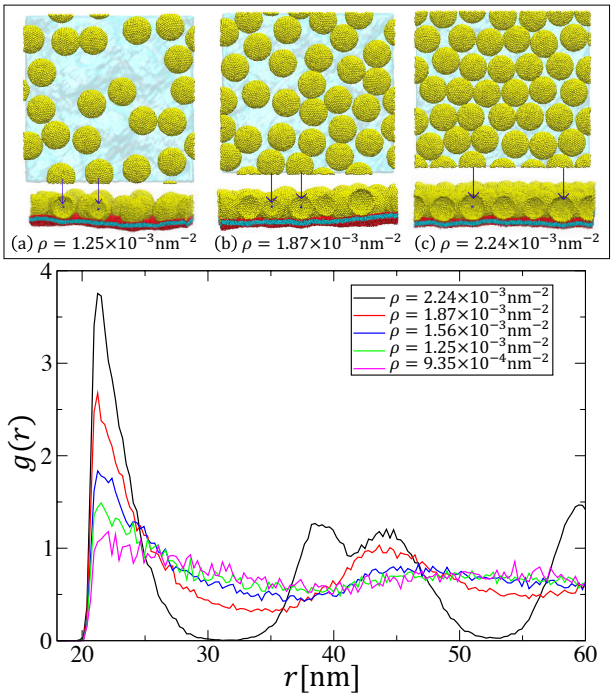

Fig. 6 (Top panel) Top and side views of equilibrium configurations of the membrane with uniform NPs for three density values at $\xi = 0.43\,k_BT/\text{nm}^2$. The area of the bare membrane is $16040\,\text{nm}^2$ for the three snapshots. The radial distribution function of the uniform NPs' centers of mass at different values of ρ at $\xi = 0.43\,k_BT/\text{nm}^2$.

3.2 Hexagonal Ordering of the Janus Nanoparticles

An exciting feature of the phase diagram in Fig. 2, is the presence of an ordered phase (solid blue triangles), in which the JNPs form a hexagonal lattice, with an example snapshot shown in Fig. 2(e). This phase occurs at intermediate values of the density and over a wide range of values of the adhesion energy density at which the degree of wrapping of each JNP is controlled by the Janusity, as shown in Fig. 1. The emergence of the hexagonal phase with increasing density is demonstrated by snapshots (a-c) in Fig. 5. The radial distribution function (RDF), $g(r)$, of the JNPs centers of mass, at $\xi = 4.11\,k_BT/\text{nm}^2$ and $\rho = 4.66\times10^{-4}$ nm^{-2}, exhibits three well-defined peaks, with the ratio between the positions of the second and first peaks, $r_2/r_1 = 1.74$, and that between the third and first peaks, $r_3/r_1 = 2.02$, are very close to those of an ideal hexagonal lattice, corresponding respectively to $\sqrt{3}$ and 2. In contrast, the RDFs at lower densities, namely at $\rho = 2.33\times10^{-4}$ nm^{-2} and $\rho = 3.11\times10^{-4}$ nm^{-2}, shown in Fig. 5(B), exhibit broader peaks in line with the disordered nature of these structures. Fig. S3 (ESI†) indicates that the dependence of the RDF of the hexagonal structure at a given density is weak. This is simply because, at high ξ, the degree of wrapping is determined mainly by the Janusity.

Since the JNPs are dispersed over the whole membrane, due to the effective repulsive interaction between them, the average distance between nearest neighbor JNPs, i.e., the position of the first peak of the RDF, is given by $r_1 = \alpha\sqrt{\mathscr{A}_0/n}$. Here, $\mathscr{A}_0$ is the membrane's projected area, and α is some dimensionless positive proportionality constant. Since the degree of wrapping of the JNPs at high adhesion energy density is determined by their Janusity, $\mathscr{A}_0 = \mathscr{A} - na$, where $\mathscr{A}$ is the projected area of the bare membrane, and a is the loss in projected area per JNP due to wrapping. a should be independent or weakly dependent on the JNP density. Therefore, the length scale $r_1 = \alpha\sqrt{1/\rho - a}$. Fig. 5(C) shows that this relation fits well the value of r_1 found in the simulations, regardless whether the JNPs are in the disordered or hexagonal phase. Therefore, due to the effective membrane-mediated repulsion between the JNPs, the lattice constant of the hexagonal phase is determined by their number density.

Hexagonal self-assembly of the JNPs occurs at $3.55\times10^{-4}\,\text{nm}^{-2} \lesssim \rho \lesssim 5\times10^{-4}\,\text{nm}^{-2}$ and $\xi \gtrsim 2k_BT/\text{nm}^2$. For $\rho \gtrsim 5\times10^{-4}\,\text{nm}^{-2}$, the membrane cannot accommodate all JNPs, which adhere to it into a hexagonal superlattice since this lattice would have a small lattice constant. Therefore, the membrane must be highly curved in the interstitial regions. The resulting excess curvature energy is relieved by the aggregation of a fraction of the JNPs into small clusters, including trimers, tetramers, etc., and their endocytosis. This reduces the lateral density of the remaining non-endocytosed JNPs on the membrane, which are self assembled into a hexagonal lattice, as shown by an example snapshot in Fig S4 (ESI†).

We emphasize that earlier molecular dynamics simulations of spherical NPs with uniform surfaces adhering to planar lipid membranes[32,54] showed that the NPs can self-assemble into linear chains. Two-dimensional self-assembly of uniform NPs into hexagonal lattices was observed by Šarić and Cacciuto.[29] However, in their study, membranes are modeled as dynamically triangulated surfaces with conserved topology, and the hexagonal lattices are observed either at high adhesion energy density, at which the NPs would endocytose, or at values of the bending modulus that are much higher than that of a typical lipid membrane in the fluid phase. Furthermore, their free energy calculations show that the NPs' linear assembly is more stable than the hexagonal self-assembly.[29] Hexagonal self-assembly of uniform spherical NPs was not observed in molecular dynamics simulations, where endocytosis is allowed[32,54]

Hexagonal self-assembly of uniform spherical NPs is possible at high densities and low values of the adhesion energy density, at which the NPs are weakly wrapped, as shown by snapshot (c) in Fig. 6 at $\rho = 2.24\times10^{-3}\,\text{nm}^{-2}$ and its corresponding RDF in the same figure. However, this self-assembly results from the NPs' crowding, as demonstrated by the fact that the RDF's first peak is at $r_1 \approx D + 1$ nm and is akin to the hexagonal ordering of hard disks. Furthermore, the large overlap between the second and third peaks of the RDF at high densities implies that the hexagonal lattice, in this case, is not as ordered as that of the Janus NPs (Fig. 5). Fig. 6 shows that the hexagonal order is lost with decreasing density. The Janus character of JNPs is, therefore, a necessary ingredient for their self-assembly into hexagonal superlattices.

To further characterize the nature of the phase transition from the disordered monomeric phase to the hexagonal phase, we calculated the six-fold bond-orientational order parameter, defined

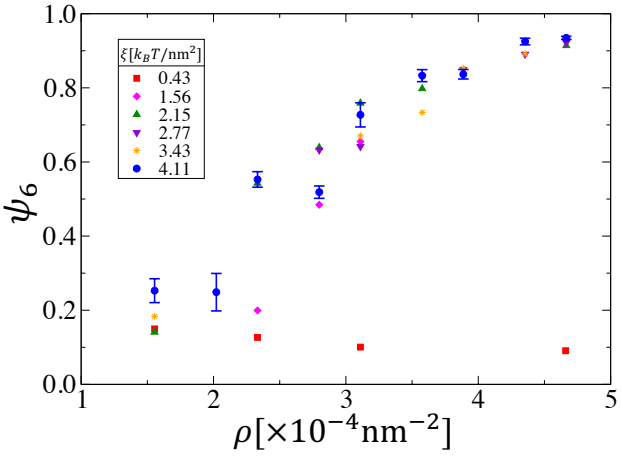

Fig. 7 Six-fold bond-orientational order parameter, ψ_6, defined in Eq. (10), as a function of the density of the JNPs at different values of ξ.

as

$$\psi_6 = \frac{1}{n}\sum_{j=1}^{n}\langle|\phi_{6j}|\rangle, \tag{10}$$

where the brackets indicate an ensemble average, and

$$\phi_{6j} = \frac{1}{n_j}\sum_{k=1}^{n_j} e^{6i\theta_{jk}} \tag{11}$$

is the local bond-orientational order parameter. In Eq. (11), the sum is over all the n_j nearest neighbors of JNP j, obtained from the 2D Delaunay triangulation based on the JNPs' center beads. θ_{jk} is the angle between an arbitrary reference axis on the xy-plane and the vector $\mathbf{R}_{jk}$ connecting the center bead of JNP j with that of its kth nearest neighbor. Fig. 7 shows that ψ_6 is low for all density values at $\xi = 0.43\,k_BT/\mathrm{nm}^2$. This is expected since for low values of the adhesion energy density, the JNPs are in the disordered state, as shown by the phase diagram in Fig. 2. In contrast, ψ_6 increases monotonically with ρ for $\xi \gtrsim 1.5\,k_BT/\mathrm{nm}^2$, and is close to 1 at high densities, which is indicative of the JNPs being crystallized into a hexagonal superlattice. It is interesting to note that the dependence of ψ_6 on ξ, at intermediate to high values of ξ, is weak. As stated earlier, this is because in this range of values of ξ, the Janusity dominates the degree of wrapping.

Since the JNPs adhering to a planar lipid membrane form a quasi-2D monolayer, one expects that their phase transition from the hexagonal phase to the disordered phase, with decreasing density, proceeds through a two-stage melting scenario via two continuous transitions, with an intermediate phase known as the hexatic phase, in line with the Kosterlitz-Thouless-Halperin-Nelson-Young (KTHNY) theory.[41–44] The crystalline phase should exhibit long-range bond-orientational order but only quasi-long-range translational order, in line with the Mermin-Wagner theorem.[55,56] The quasi-long-range translational order of the crystalline phase is due to thermally induced dislocation defects, which are bound in pairs. The first step of melting proceeds through the dissociation of these dislocation pairs resulting in an intermediate phase, known as the hexatic phase that retains quasi-long-range bond-orientational order but lacks long-range translational order. The hexatic phase is characterized by the presence of bound disclination pairs. With a decrease in the density, these disclination pairs unbind, leading to the transition of the hexatic phase into the disordered (isotropic) phase, which lacks both translational and bond-orientational order. The nature of the melting transition of the JNPs system can, therefore, be inferred from either the long wavelength decay of the translational or the bond-orientational correlation functions. However, an unambiguous characterization of the long-wavelength decay of these correlation functions would require simulations of very large membranes with a large number of adhering JNPs, which is not achievable with current computational resources. Instead, we quantified the melting behavior of the JNPs' hexagonal phase with decreasing density through two quantities corresponding to the dynamical 2D Lindemann parameter and the bond-orientational autocorrelation function.

The 2D dynamical Lindemann parameter, which is a measure of the relative neighbor-neighbor displacement, introduced by Bedanov and Gadiyak[57] and later modified by Zahn *et al.*,[58] is defined as

$$\begin{aligned}\gamma_L(t) &= \frac{1}{2r_1^2}\langle[\Delta\mathbf{R}_{rel}(t)]^2\rangle \\ &= \frac{1}{2r_1^2}\left\langle\frac{1}{\sum_{j=1}^{n} n_j(t_0)}\sum_{j=1}^{n}\sum_{k=1}^{n_j(0)}\left[\mathbf{R}_{jk}(t+t_0)-\mathbf{R}_{jk}(t_0)\right]^2\right\rangle,\end{aligned} \tag{12}$$

where j and k are nearest neighbor JNPs at time t_0, as determined from the 2D Delaunay triangulation at t_0, and $\mathbf{R}_{jk}(t) = \mathbf{R}_j(t) - \mathbf{R}_k(t)$, where $\mathbf{R}_j(t)$ and $\mathbf{R}_k(t)$ are the coordinates of the center beads of JNPs j and k, respectively, at time t. In the crystalline phase, $\gamma_L(t)$ converges asymptotically to a constant value since particles are bound in this phase. In the liquid phase, however, the positions of initially neighboring particles become uncorrelated at late times, leading to a divergence of γ_L. At the melting point, $\gamma_L(t)$ approaches a critical value $\gamma_L^c \approx 0.033$[58]. Fig. 8(A) depicts $\gamma_L(t)$ of the JNPs for different values of the density ρ. This figure shows that for low values of ρ, γ_L diverges, indicating a disordered liquid phase. However, at $\rho \gtrsim 3.5\times10^{-4}\,\mathrm{nm}^{-2}$, γ_L converges to a constant that increases with ρ but is smaller than γ_L^c. This indicates that the melting of the JNPs' hexagonal crystal must happen at some density $3.11\times10^{-4}\,\mathrm{nm}^{-2} < \rho^* < 3.58\times10^{-4}\,\mathrm{nm}^{-2}$.

While the dynamical Lindemann criterion, discussed above, is used to determine the melting transition of the hexagonal crystal, it cannot be used to determine the transition from the hexatic phase to the liquid phase. This transition is inferred from the bond-orientational autocorrelation function, defined as,

$$g_6(t) = \frac{1}{n}\sum_{j=1}^{n}\langle\phi_{6j}^*(t+t_0)\cdot\phi_{6j}(t_0)\rangle, \tag{13}$$

where ϕ_{6j} was defined in Eq. (11). Fig. 8(B) shows $g_6(t)$ in a double logarithmic plot for different density values at $\xi = 4.11\,k_BT/\mathrm{nm}^2$. This figure shows that $g_6(t)$ exhibits three distinct regimes. At low densities ($\rho \lesssim 2.0\times10^{-4}\,\mathrm{nm}^{-2}$), g_6 decays exponentially. This implies that the JNPs are in a disordered (liquid)

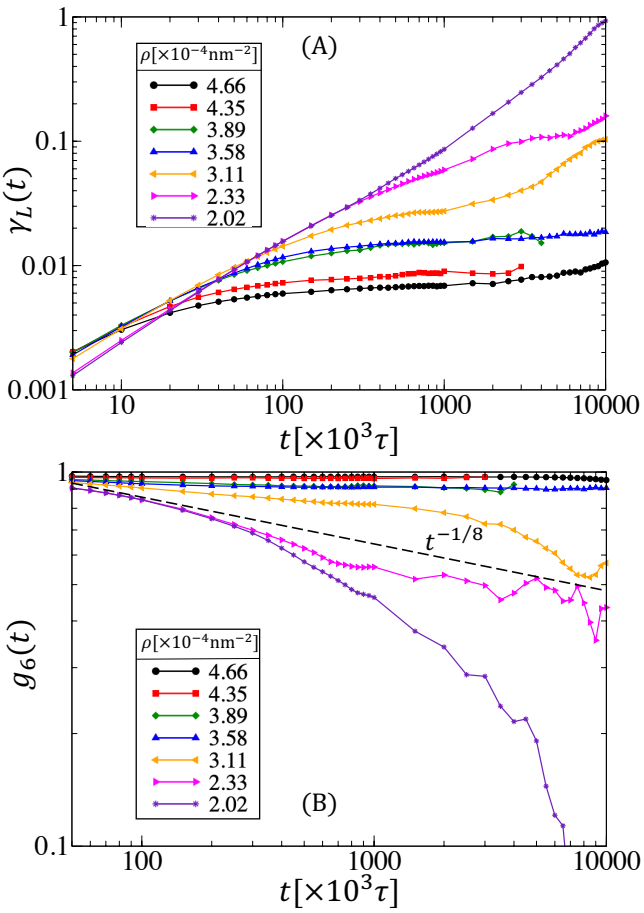

Fig. 8 (A) The dynamic Lindemann parameter for different density values versus time. (B) The bond-orientational autocorrelation function for different density values. The slope of the dashed black line in (B) corresponds to the transition from the hexatic to the liquid phase, as predicted by KTHNY theory.

state at low densities. In contrast, g_6 converges to a constant value at $\rho \gtrsim 3.5\times10^{-4}\,\mathrm{nm}^{-2}$, which indicates that the JNPs are in the crystalline hexagonal phase at high densities. This range of densities over which the JNPs are self-assembled into a hexagonal lattice agrees with that obtained from the Lindemann parameter, shown in Fig. 8(A). Interestingly, Fig. 8(B) shows a regime, at intermediate densities, *e.g.*, $\rho = 2.33\times10^{-4}\,\mathrm{nm}^{-2}$, in which g_6 seems to decay algebraically, i.e., $g_6(t) \sim t^{-\eta_r}$. This hints at the existence of a phase that exhibits quasi-long-range bond-orientational order, i.e., the hexatic phase. KTHNY theory predicts that the spatial bond-orientational correlation function decays exponentially, $g_6(r) \sim t^{-\eta_{6,r}}$, with η_r where $\eta_{6,r} = 2\eta_{6,t}$.[43,59] Furthermore, KTHNY's theory predicts that the exponent $\eta_{6,r} = 1/4$ at the hexatic-liquid transition, and this exponent decreases to zero within the hexatic phase as the hexatic-crystal transition is approached. Fig. 8(B) shows that at $\rho = 2.33\times10^{-4}\,\mathrm{nm}^{-2}$, the exponent of the algebraic decay of $\eta_{6,t} \approx 1/8$, which in fair agreement with KTHNY theory. This indicates that the hexatic-isotropic transition probably occurs at $\rho \approx 2.3\times10^{-4}\,\mathrm{nm}^{-2}$, although more simulations would be needed to determine the density corresponding to this transition accurately. Nevertheless, our aim is to demonstrate that the JNPs exhibit a hexatic phase at intermediate densities. It is noted that the calculations of both Lindemann parameter and bond-orientational autocorrelation functions require very long, computationally expensive simulations. As a result, the data shown in Fig. 8(A) and (B) do seem to deviate from their expected behavior at large t values ($t \gtrsim 4000\tau$). This is attributed to poor statistics.

4 Conclusions

Using molecular dynamics simulations of a coarse-grained implicit-solvent model, we showed that Janus nanoparticles exhibit a range of phases on planar lipid membranes. These correspond to a disordered phase, in which the JNPs are apart at low values of the adhesion energy density, ξ, or number density, ρ. At low values of ξ, the JNPs self-assemble into linear chains at intermediate ρ, then into tubular chains at higher values of ρ. At high values of ρ and intermediate to high values of ξ, a fraction of the JNPs are endocytosed. The most striking structure exhibited by the JNPs on lipid membranes is an ordered self-assembled hexagonal lattice at intermediate values of ρ and intermediate and high values of ξ. This phase occurs when a JNP's degree of wrapping becomes mainly controlled by its Janusity. The lattice constant of the hexagonal phase is determined by the JNPs' number density on the membrane. The nature of the melting behavior of the hexagonal lattice, with decreasing density, is inferred from several quantities, including the 2D Lindemann parameter and the bond-orientational autocorrelation function. Owing to the quasi-2D nature of the system, we found that the hexagonal lattice melts through a two-stage scenario with decreasing ρ, in agreement with the KTHNY theory of 2D melting. Namely, the hexagonal lattice first melts into a hexatic phase, characterized by a power-law decay with time of the autocorrelation function. With a further decrease of the density, the hexatic phase melts into the disordered liquid phase, which is characterized by an exponential decay of the autocorrelation function.

The emergence of the ordered hexagonal lattice of the JNPs on the membrane, with a lattice constant that is determined by their density, is due to a repulsive interaction between the JNPs that is mediated by the curvature of the membrane, as shown by the free energy calculation using the weighted histogram analysis method. This hexagonal lattice is simply the asymptotic limit of the highly ordered nanoassemblies of Janus NPs on lipid vesicles, recently observed by us.[40] There, we found that the JNPs self-assemble into highly ordered polyhedra on vesicles, including three Platonic solids, with geometries that satisfy the upper limit of Euler's polyhedral formula.

We note that the present study is focused on JNPs with one specific diameter, corresponding to 20 nm, and one specific Janusity, corresponding to 0.5. The effect of the diameter should be relatively minimal, except that the adhesion strength values in the phase diagram of Fig. 2 will be shifted to lower values with increasing diameter[38,40]. The Janusity is also expected to affect the phase diagram. Namely, we expect the transition density from the liquid to the hexagonal phase to increase with the Janusity. We plan to investigate these effects systematically in the future. The collective behavior of the JNPs at intermediate values of the adhe-

sion strength, namely the aggregation of the JNPs into linear in-plane or tubular chains, remains intriguing and begs for further investigation. This behavior is outside the scope of the present study. Due to the relatively large size of the JNPs (diameter of 20 nm) in the current study, simulations of membranes with a large number of JNPs would require a substantial computational effort beyond our capabilities. However, we believe that our results will remain valid for large systems. Future larger-scale simulations are warranted to validate the observed hexagonal order of the JNPs and the presence of a hexatic phase at intermediate densities.

The self-assembly of these JNPs on planar membranes is fundamentally different from that of uniform spherical NPs, which do not exhibit hexagonal order,[54] except at high values of ρ and low values of ξ. This structure is however the result of crowding of the NPs on the membrane. In the case of NPs with uniform surfaces, decreasing their density on the membrane leads to the melting of the hexagonal lattice.

To our knowledge, experimental studies investigating the adhesion of hydrophilic JNPs to lipid membranes have yet to be conducted. Such studies would be instrumental in validating our computational results. The results of the present study, in combination with those in Ref.[40] are very exciting and open up a door for the potential use of planar lipid membranes and lipid vesicles as a medium for bottom-up nanofabrication of ordered structures.

Conflicts of interest

There are no conflicts of interest to declare.

Acknowledgements

This work was supported by a grant from the National Science Foundation (DMR-1931837). The simulations were performed on computers of the High Performance Computing Facility at the University of Memphis. This research used resources of the Oak Ridge Leadership Computing Facility, which is a DOE Office of Science User Facility supported under Contract DE-AC05-00OR22725. Snapshots in this article were generated using VMD version 1.9.3.[60]

Notes and references

1 S. Kundu and A. Patra, *Chem. Rev.*, 2017, **117**, 712–757.
2 P. Xiong, Y. Wu, Y. Liu, R. Ma, T. Sasaki, X. Wang and J. Zhu, *Energy Environ. Sci.*, 2020, **13**, 4834–4853.
3 J.-M. Lamarre, F. Billard, C. H. Kerboua, M. Lequime, S. Roorda and L. Martinu, *Opt. Comm.*, 2008, **281**, 331–340.
4 X. Wu, C. Hao, J. Kumar, H. Kuang, N. A. Kotov, L. M. Liz-Marzán and C. Xu, *Chem. Soc. Rev.*, 2018, **47**, 4677–4696.
5 C. Yu, X. Guo, M. Shen, B. Shen, M. Muzzio, Z. Yin, Q. Li, Z. Xi, J. Li, C. T. Seto and S. Sun, *Ang. Chem. Int. Ed.*, 2018, **57**, 451–455.
6 S. Kumar, A. Daverey, V. Khalilzad-Sharghi, N. K. Sahu, S. Kidambi, S. F. Othman and D. Bahadur, *RSC Adv.*, 2015, **5**, 53180–53188.
7 M. J. Mitchell, M. M. Billingsley, R. M. Haley, M. E. Wechsler, N. A. Peppas and R. Langer, *Nat. Rev. Drug Discov.*, 2021, **20**, 101–124.
8 M. S. M. Saifullah, M. Asbahi, D. C. J. Neo, Z. Mahfoud, H. R. Tan, S. T. Ha, N. Dwivedi, T. Dutta, S. bin Dolmanan, Z. Aabdin, M. Bosman, R. Ganesan, S. Tripathy, D. G. Hasko and S. Valiyaveettil, *Nano Lett.*, 2022, **22**, 7432–7440.
9 A. V. Kabashin and M. Meunier, *J. Appl. Phys.*, 2003, **94**, 7941–7943.
10 L. Yang, J. Wei, Z. Ma, P. Song, J. Ma, Y. Zhao, Z. Huang, M. Zhang, F. Yang and X. Wang, *Nanomaterials*, 2019, **9**, 1789.
11 H. Kang, F. A. Detcheverry, A. N. Mangham, M. P. Stoykovich, K. C. Daoulas, R. J. Hamers, M. Müller, J. J. de Pablo and P. F. Nealey, *Phys. Rev. Lett.*, 2008, **100**, 148303.
12 M. Stevens, N. Flynn, C. Wang, D. Tirrell and R. Langer, *Adv. Mater.*, 2004, **16**, 915–918.
13 K. L. Gurunatha, A. C. Fournier, A. Urvoas, M. Valerio-Lepiniec, V. Marchi, P. Minard and E. Dujardin, *ACS Nano*, 2016, **10**, 3176–3185.
14 T. A. T. Lee, A. Cooper, R. P. Apkarian and V. P. Conticello, *Adv. Mater.*, 2000, **12**, 1105–1110.
15 Y. Fan, Y. Liu, Y. Wu, F. Dai, M. Yuan, F. Wang, Y. Bai and H. Deng, *Int. J. Biol. Macromol.*, 2021, **192**, 1240–1255.
16 M. Rahimi, T. F. Roberts, J. C. Armas-Pérez, X. Wang, E. Bukusoglu, N. L. Abbott and J. J. de Pablo, *Proceedings of the National Academy of Sciences*, 2015, **112**, 5297–5302.
17 C. A. Mirkin, R. L. Letsinger, R. C. Mucic and J. J. Storhoff, *Nature*, 1996, **382**, 607–609.
18 R. Veneziano, S. Ratanalert, K. Zhang, F. Zhang, H. Yan, W. Chiu and M. Bathe, *Science*, 2016, **352**, 1534–1534.
19 P. Kühler, E.-M. Roller, R. Schreiber, T. Liedl, T. Lohmüller and J. Feldmann, *Nano Lett.*, 2014, **14**, 2914–2919.
20 E.-M. Roller, L. V. Besteiro, C. Pupp, L. K. Khorashad, A. O. Govorov and T. Liedl, *Nature Phys.*, 2017, **13**, 761–765.
21 M. Pilo-Pais, A. Watson, S. Demers, T. H. LaBean and G. Finkelstein, *Nano Lett.*, 2014, **14**, 2099–2104.
22 K. Matsuura, G. Ueno and S. Fujita, *Polym. J.*, 2015, **47**, 146–151.
23 L. Xu, W. Yan, W. Ma, H. Kuang, X. Wu, L. Liu, Y. Zhao, L. Wang and C. Xu, *Adv. Mat.*, 2015, **27**, 1706–1711.
24 M. J. Urban, P. K. Dutta, P. Wang, X. Duan, X. Shen, B. Ding, Y. Ke and N. Liu, *J. Am. Chem. Soc.*, 2016, **138**, 5495–5498.
25 W. Chen, A. Bian, A. Agarwal, L. Liu, H. Shen, L. Wang, C. Xu and N. A. Kotov, *Nano Lett.*, 2009, **9**, 2153–2159.
26 P. Kumar, T. Vo, M. Cha, A. Visheratina, J.-Y. Kim, W. Xu, J. Schwartz, A. Simon, D. Katz, V. P. Nicu, E. Marino, W. J. Choi, M. Veksler, S. Chen, C. Murray, R. Hovden, S. Glotzer and N. A. Kotov, *Nature*, 2023, **615**, 418–424.
27 L. F. Kadem, C. Lamprecht, J. Purtov and C. Selhuber-Unkel, *Langmuir*, 2015, **31**, 9261–9265.
28 A. Šarić and A. Cacciuto, *Phys. Rev. Lett.*, 2012, **109**, 188101.
29 A. Šarić and A. Cacciuto, *Phys. Rev. Lett.*, 2012, **108**, 118101.
30 A. H. Bahrami, R. Lipowsky and T. R. Weikl, *Phys. Rev. Lett.*, 2012, **109**, 188102.

31 C. van der Wel, A. Vahid, A. Šarić, T. Idema, D. Heinrich and D. J. Kraft, *Sci. Rep.*, 2016, **6**, 32825.

32 K. Xiong, J. Zhao, D. Yang, Q. Cheng, J. Wang and H. Ji, *Soft Matter*, 2017, **13**, 4644–4652.

33 E. J. Spangler, P. B. S. Kumar and M. Laradji, *Soft Matter*, 2018, **14**, 5019–5030.

34 E. J. Spangler and M. Laradji, *J. Chem. Phys.*, 2021, **154**, 244902.

35 A. Sharma, Y. Zhu, E. J. Spangler, J.-M. Y. Carrillo and M. Laradji, *Soft Matter*, 2023, **19**, 1499–1512.

36 J. Midya, T. Auth and G. Gompper, *ACS Nano*, 2023, **17**, 1935–1945.

37 A. H. Bahrami and T. R. Weikl, *Nano Lett.*, 2018, **18**, 1259–1263.

38 Y. Zhu, A. Sharma, E. J. Spangler and M. Laradji, *Soft Matter*, 2022, **18**, 4689–4698.

39 D. S. Richeson, *Euler's Gem: The Polyhedron Formula and the Birth of Topology*, Princeton University Press, 2008.

40 Y. Zhu, A. Sharma, E. J. Spangler, J.-M. Y. Carrillo, P. B. S. Kumar and M. Laradji, *Soft Matter*, 2023, **19**, 2204–2213.

41 J. M. Kosterlitz and D. J. Thouless, *J. Phys. C: Solid State Phys.*, 1973, **6**, 1181–1203.

42 B. I. Halperin and D. R. Nelson, *Phys. Rev. Lett.*, 1978, **41**, 121–124.

43 D. R. Nelson and B. I. Halperin, *Phys. Rev. B*, 1979, **19**, 2457–2484.

44 A. P. Young, *Phys. Rev. B*, 1979, **19**, 1855–1866.

45 J. D. Revalee, M. Laradji and P. B. Sunil Kumar, *J. Chem. Phys.*, 2008, **128**, 035102.

46 M. Laradji, P. B. Sunil Kumar and E. J. Spangler, *J. Phys. D: Appl. Phys.*, 2016, **49**, 293001.

47 J. R. Baumgardner and P. O. Frederickson, *SIAM J. Num. Anal.*, 1985, **22**, 1107–1115.

48 J. F. Nagle, M. S. Jablin, S. Tristram-Nagle and K. Akabori, *Chem. Phys. Lipids*, 2015, **185**, 3–10.

49 N. Kučerka, S. Tristram-Nagle and J. F. Nagle, *Biophysical Journal*, 2006, **90**, L83–L85.

50 A. Sharma, Y. Zhu, E. J. Spangler and M. Laradji, *J. Chem. Phys.*, 2022, **156**, 234901.

51 G. S. Grest and K. Kremer, *Phys. Rev. A*, 1986, **33**, 3628–3631.

52 W. C. Swope, H. C. Andersen, P. H. Berens and K. R. Wilson, *J. Chem. Phys.*, 1982, **76**, 637–649.

53 S. Kumar, J. M. Rosenberg, D. Bouzida, R. H. Swendsen and P. A. Kollman, *J. Comp. Chem.*, 1992, **13**, 1011–1021.

54 E. J. Spangler, P. B. Sunil Kumar and M. Laradji, *Soft Matter*, 2018, **14**, 5019–5030.

55 N. D. Mermin and H. Wagner, *Phys. Rev. Lett.*, 1966, **17**, 1133–1136.

56 N. D. Mermin, *Phys. Rev.*, 1968, **176**, 250–254.

57 V. Bedanov, G. Gadiyak and Y. Lozovik, *Phys. Lett. A*, 1985, **109**, 289–291.

58 K. Zahn, R. Lenke and G. Maret, *Phys. Rev. Lett.*, 1999, **82**, 2721–2724.

59 J. M. Kosterlitz, *J. Phys. C: Solid State Phys.*, 1974, **7**, 1046–1060.

60 W. Humphrey, A. Dalke and K. Schulten, *J. Mol. Graph.*, 1996, **14**, 33–38.